remote sensing

MDPI

Article

Sparse VLF/LF Lightning Location: Propagation Correction and Accelerating-Charge-Based Peak-Field Consistency

Yiyun Xia, Yunfeng Zhang * and Boxiong Weng

School of Electronics and Information Engineering, Nanjing University of Information Science & Technology, Nanjing 210044, China; 202512492580@nuist.edu.cn (Y.X.); 202512491071@nuist.edu.cn (B.W.)
* Correspondence: zhangyunfeng@nuist.edu.cn

Highlights

What are the main findings?

- Given known ground conductivity, peak arrival-time shifts and amplitude changes are corrected separately: time correction improves TDOA location accuracy, while amplitude correction recovers multistation peaks for ACM consistency testing.
- Once candidate locations are fixed, ACM peak electric field consistency distinguishes correct and spurious solutions in the controlled in-network test, the out-of-network simulation, and the rocket-triggered lightning case.

What are the implications of the findings?

- Three-station peak arrival times and amplitudes support separate stages for location correction and candidate discrimination without requiring additional stations.
- More reliable lightning locations can support the spatial analysis of thunderstorm electrical activity, severe-convection studies, and joint applications with radar and satellite observations.

Abstract

Sparse very-low-frequency/low-frequency (VLF/LF) lightning location is a ground-based passive remote-sensing technique, but sparse station geometry and finite-conductivity propagation can shift peak arrival times, alter peak amplitudes, and produce spurious solutions. This study proposes a three-station method integrating propagation correction with accelerating charge method (ACM)-based peak-electric-field consistency. Based on the Liénard–Wiechert field, the ACM relates the radiation field to charge acceleration and assumes a common source-side peak for the same return stroke. For given ground conductivity, relative permittivity, and an ACM reference field, the range-dependent additional delay τ_E corrects TDOA to obtain candidate locations. After candidate coordinates are fixed, the peak-retention factor A_E, candidate-to-station distances, and local response K_i recover equivalent source-side peaks, while J_{amp} discriminates between correct and spurious candidates. In simulations, the in-network location error decreased from 46.0 to 21.8 m and the out-of-network error from 1867.3 to 394.8 m; the ACM-based criterion selected the correct candidate in both cases. For the S7–S8–S9 rocket-triggered-lightning case, the near-candidate error decreased from 1.333 to 0.360 km, and J_{amp} values of 0.0419 and 0.2238 distinguished the correct and spurious solutions. The method therefore improves sparse VLF/LF lightning location accuracy through propagation-time correction and supports spurious-solution discrimination through propagation-corrected peak-field consistency.

Check for updates

Academic Editor: Michael E. Gorbunov

Received: 16 August 2026
Revised: 21 October 2026
Accepted: 22 October 2026
Published: 24 October 2026

Copyright: © 2026 by the authors. Licensee MDPI, Basel, Switzerland. This article is an open access article distributed under the terms and conditions of the Creative Commons Attribution (CC BY) license.

Keywords: VLF/LF lightning location; time difference of arrival; accelerating charge method; peak electric field consistency; propagation correction; rocket-triggered lightning; multiple-solution discrimination

1. Introduction

Lightning return strokes produce very-low-frequency/low-frequency (VLF/LF) electromagnetic pulses that propagate over long distances. By retrieving discharge locations from multistation observations, VLF/LF lightning location provides a ground-based passive remote-sensing tool for atmospheric electrical activity. It supports severe-convection monitoring, thunderstorm analysis, and lightning-protection assessment [1,2], as well as coordinated observations with radar, satellites, and other meteorological sensors. Ground-based lightning location networks typically receive electromagnetic pulses synchronously and infer strike locations from interstation time differences of arrival. With sparse stations or sources near or outside the network boundary, however, the results are sensitive to network geometry, noise, and propagation conditions [1–8]. During VLF/LF ground-wave propagation, surface electrical properties, terrain, and propagation paths can shift peak times, attenuate amplitudes, and broaden wavefronts [9–13]. Dowden et al. extracted group arrival times from the phase–frequency relationship of VLF waveforms [14]; Said et al. used a waveform bank and template matching for long-range location [15]; Xu et al. combined LWPC and IRI models to estimate path group velocities [16]; and Zhang et al. improved location results by compensating for ground-wave delays [17]. These studies primarily address arrival-time extraction and propagation modeling. The consistency of multistation peak electric fields with a common radiation source remains less fully exploited.

TDOA uses only interstation arrival-time differences. Three stations are the minimum configuration for two-dimensional location, and a timing error at any station can displace the intersection of the constraint hyperbolas. Near or outside the network boundary, the hyperbolas often intersect at a small angle, amplifying timing errors geometrically. Location accuracy depends on the number and layout of participating stations, the strike position, and synchronization and propagation errors [6,7,18,19]. Conventional TDOA also makes limited use of peak electric fields. When two candidates satisfy the same time-difference constraints, timing alone may not identify which better represents the physical radiation process.

Using waveform information beyond geometric timing constraints requires an understanding of how the received electric field relates to the lightning source. Conventional return-stroke field calculations start from channel current or current density and calculate the electromagnetic fields generated as the current pulse travels along the channel [20–24]. Here, we use the term accelerating charge method (ACM) for return-stroke field calculations based on the field expressions of moving and accelerating charges. This formulation interprets channel current in terms of charge motion and acceleration. Cooray et al. demonstrated the physical equivalence of current-based and charge-acceleration-based calculations [20–23,25]. The ACM thus provides a physical basis for common source-side radiation from a single event. Differences among station peaks mainly reflect distance, propagation loss, station response, and noise, providing the basis for a peak electric field consistency criterion.

Transmission-line models and their variants calculate return-stroke far fields and channel currents from a prescribed channel-base current, return-stroke speed, height-dependent attenuation, and propagation assumptions. Even with the same base current, different

propagation assumptions yield different current distributions and far-field waveforms [26]. Results also depend on channel segmentation, per-unit-length parameters, and boundary conditions [27]. Retrieving these source and path parameters for each location estimate would increase the number of unknowns and the computational cost, while making source and propagation effects difficult to separate.

The ACM directly relates radiation to charge acceleration. In Liénard–Wiechert field theory, accelerating charges generate radiation fields [20,21,25,28,29], allowing common source radiation to be distinguished from station-dependent propagation effects. This separation offers three advantages for location. First, only the peak arrival time and peak electric field are needed for each event, without retrieving the complete channel current, return-stroke speed, or height distribution. Second, TDOA constrains range differences, whereas peak fields contain information about absolute distances. Third, after the timing branch independently generates candidates, A_{E} and local station responses recover equivalent source-side peaks whose consistency is tested by the ACM. Thus, the ACM discriminates among candidates, while propagation-time correction reduces location bias.

This study addresses two problems in sparse three-station VLF/LF lightning location: spatial ambiguity caused by multiple TDOA candidates, and the peak-time shifts and amplitude changes caused by finitely conducting ground. The latter require separate timing and amplitude corrections to support candidate location and consistency testing [9–13,17,30–33]. We combine TDOA geometry, conductivity-based propagation correction, and ACM peak electric field consistency. Given the regional equivalent ground conductivity σ, the additional peak delay $\tau_{\mathrm{E}}(\mathrm{R},\sigma)$ and peak-retention factor $A_{\mathrm{E}}(\mathrm{R},\sigma)$ are calculated as functions of distance. The delay corrects TDOA range differences to generate candidate coordinates. The amplitude branch then uses $A_{\mathrm{E}}(\mathrm{R},\sigma)$, the local response K_{i}, and candidate-to-station distances to recover equivalent source-side peaks. The ACM residual J_{amp} distinguishes correct and spurious solutions. The propagation response is calculated using the Wait surface-impedance model in Section 2.3.

Section 2 presents the theoretical basis of ACM peak electric field consistency, TDOA candidate formulation, and propagation correction based on ground electrical properties. Section 3 examines in-network and out-of-network scenarios, reports three sets of Monte Carlo experiments with timing, amplitude, and joint perturbations, and validates location correction and candidate discrimination using S7–S8–S9 rocket-triggered lightning data. Section 4 discusses the roles of the simulations and observations, the limits of the propagation model, and the significance of the measured results. Section 5 presents the conclusions.

2. Theory and Methods

2.1. Accelerating-Charge Radiation and Peak Electric Field Consistency

At VLF/LF frequencies, distant return-stroke signals recorded by wide-area lightning location networks can be interpreted in terms of rapid charge acceleration within the channel. For an approximately vertical channel and a ground-based far-field observation direction nearly perpendicular to charge motion, the dominant radiation term of a single accelerating charge follows from the Liénard–Wiechert field [20–24]

$$\mathbf{E}_{rad}(\mathbf{r},t) = \left.\frac{q}{4\pi\varepsilon_0 c^2 R}\,\hat{\mathbf{e}}_R \times (\hat{\mathbf{e}}_R \times \dot{\mathbf{u}})\right|_{t'=t-R/c}. \tag{1}$$

In Equation (1), $\mathbf{E}_{\mathrm{rad}}$ is the radiation electric field, $\mathbf{r}$ is the observation position, t is the observation time, q is the charge, ε_0 is the vacuum permittivity, c is the speed of light in vacuum, R is the distance from the charge to the observer, $\hat{\mathbf{e}}_R$ is the corresponding unit vector, $\mathbf{u}$ and $\dot{\mathbf{u}}$ are the charge velocity and acceleration, and $t' = t - R/c$ is the retarded time. This projection approximation requires an approximately vertical channel

and horizontal source-to-station distances much greater than the height of the dominant radiating region, so that all observation directions are nearly horizontal. Its validity therefore depends on both channel height and source-to-station distances, rather than station spacing alone. Under Equation (1), if θ is the angle between the charge-to-station direction and the vertical, the angular factor of the vertical radiation field is $\sin^2\theta$. Replacing this factor by its horizontal-observation value of 1 introduces a deviation of $\cos^2\theta$ relative to that value. For example, an angular departure of no more than 10° from 90° gives a projection deviation of approximately 3% or less. This estimate applies only to the angular projection. Nearby stations or substantially inclined or tortuous channels may introduce larger interstation differences in projection and channel retardation, affecting recovered source-side peaks and J_{amp}. Incorporating channel-internal retardation into a common source-time function S(t), the far field at station i is written as

$$E_i(t) = \frac{S(t - R_i/c)}{R_i}. \quad (2)$$

In Equation (2), i denotes the station, E_i(t) is its far-field electric field, R_i is its distance from the lightning source, and S(t) is the common source-time function determined by the source-side acceleration process of the same return stroke. We extract the peak arrival time and peak electric field. Denoting the source-side peak by S_{peak} gives

$$S_{peak} = \max_t |S(t)|, \qquad \left|E_{peak,i}\right| = \frac{S_{peak}}{R_i}. \quad (3)$$

In Equation (3), S_{peak} is the source-side peak and $|E_{peak,i}|$ is the peak electric field magnitude at station i. For the same event, source-side peak consistency and interstation peak ratios therefore satisfy

$$\left|E_{peak,i}\right|R_i = \left|E_{peak,j}\right|R_j = S_{peak}, \qquad \frac{\left|E_{peak,i}\right|}{\left|E_{peak,j}\right|} = \frac{R_j}{R_i}. \quad (4)$$

In Equation (4), i and j denote different stations; and R_j and $|E_{peak,j}|$ are the source distance and peak field magnitude at station j. Different candidates imply different combinations of absolute station distances. After compensating for propagation and local station responses, the correct candidate should yield the most consistent source-side peaks.

The ACM reference field is constructed using a one-dimensional straight vertical channel and the modified transmission-line model with exponential decay (MTLE). The channel-base current follows a double-Heidler waveform with subsequent-return-stroke parameters [26,34]. The return-stroke speed is constant, and current decays exponentially with height. For the constant-speed MTLE model, the two radiation terms given by V. Cooray and G. Cooray [25] can be expressed through a common source-time function

$$S_{ACM}(t) \propto -v i_b(t) + \frac{v}{\lambda}\int_0^H i_b\left(t - \frac{z}{v}\right)e^{-z/\lambda}\,dz. \quad (5)$$

In Equation (5), S_{ACM}(t) is the ACM source-time function, i_b(t) is the channel-base current, z is height along the channel, H is channel height, v is return-stroke speed, and λ is the current-decay height. We use H = 7.5 km, v = 1.5×10^8 m/s, and λ = 2 km [26,34]. Comparison with the finite-geometry radiation terms in Equations (19) and (22) in Ref. [25] gives maximum differences of 0.28 ns in τ_E and 5×10^{-5} in A_E, indicating that the reduced representation has little effect on peak propagation characteristics.

2.2. TDOA Candidates and ACM Discrimination of Spurious Solutions

Three-station TDOA can yield multiple candidates. Here, a spurious solution is a location that satisfies the time-difference constraints but differs from the true strike point.

For the in-network scenario, the original branch g = +1 produces the correct candidate, while reversing the signs of the entire constraint set with g = −1 constructs a controlled spurious candidate. The out-of-network simulation and the rocket-triggered lightning case use only g = +1 and retain the two candidates produced by that constraint set. All candidates are ranked using the same ACM criterion after their coordinates are fixed.

With station 1 as the reference, constraints are formed from the observed arrival-time differences between the other stations and station 1. For a trial location x, the relative additional peak delays are obtained from the station distances. The propagation-corrected TDOA constraints are

$$R_i(\mathbf{x}) - R_1(\mathbf{x}) + c\,\Delta\tau_{E,i1}(\mathbf{x},\sigma) = g\,c\,\Delta t_{i1}^{obs}, \qquad i = 2,3, \quad g \in \{-1,+1\}. \tag{6}$$

In Equation (6), x is the trial location, and $R_i(x)$ and $R_1(x)$ are its distances to station i and reference station 1. $\Delta t_{i1}{}^{obs}$ is the observed peak arrival-time difference, defined as station i minus station 1; the superscript obs denotes an observation. The equivalent ground conductivity is σ, and $\Delta\tau_{E,i1}(x,\sigma)$ is the additional peak-delay difference between the two paths, in the same station order. Each path delay τ_E is obtained from the propagation response in Section 2.3, and c is the speed of light in vacuum. The common branch factor g applies to the entire constraint set: g = +1 denotes the original branch, while g = −1 reverses both range-difference constraints in the in-network test. Mixed-sign combinations are not used. For a prescribed g, bounded least squares minimizes the timing residual to obtain candidate locations.

The g = +1 and g = −1 branches are solved separately in the in-network scenario. Only g = +1 is solved for the out-of-network simulation and rocket-triggered lightning case; both candidates, when present, enter the ACM comparison. Once fixed, candidate k is denoted by $x^{(k)}$, with station distances $R_i{}^{(k)}$. Its equivalent source-side peaks are recovered as

$$\hat{S}_i^{(k)} = \frac{\left|E_{peak,i}^{obs}\right| R_i^{(k)}}{K_i\,A_E\left(R_i^{(k)},\sigma\right)}. \tag{7}$$

In Equation (7), k denotes the candidate, $S_i{}^{(k)}$ is the equivalent source-side peak recovered at station i for candidate k, $R_i{}^{(k)}$ is the corresponding distance, $|E_{peak,i}{}^{obs}|$ is the observed peak electric field magnitude, K_i is the local station peak-field response coefficient, and A_E is the peak-retention factor for the candidate path. After correcting for distance, local response, and propagation attenuation, the correct candidate should produce more consistent source-side peaks across stations.

To remove the dependence on absolute source strength, the ACM consistency residual is defined from the dispersion of the logarithmic source-side peaks

$$J_{amp}^{(k)} = \sum_{i=1}^{N}\left[\ln\hat{S}_i^{(k)} - \overline{\ln\hat{S}}^{(k)}\right]^2. \tag{8}$$

In Equation (8), $J_{amp}{}^{(k)}$ is the ACM consistency residual for candidate k, N is the number of stations (N = 3 here), and the overbar denotes the station average of the logarithmic source-side peaks. A smaller residual indicates greater agreement among the peaks recovered after propagation and station-response compensation. This quantity only ranks candidates already fixed by the timing branch.

2.3. Conductivity-Based Wait Propagation Response and Peak Corrections

A finitely conducting ground causes frequency-dependent amplitude and phase changes in lightning electromagnetic pulses [9–12]. Wait ground-wave theory describes these effects using surface impedance and the Sommerfeld attenuation function [30,31].

Shoory et al. [32] evaluated the accuracy of the approximation, and related propagation delays have been used to correct lightning locations [17]. For angular frequency ω, we define

$$\gamma_0 \equiv j\omega\sqrt{\mu_0\varepsilon_0}, \qquad \gamma_1 = \sqrt{j\omega\mu_0(\sigma + j\omega\varepsilon_0\varepsilon_r)}. \tag{9}$$

In Equation (9), γ_0 and γ_1 are the complex propagation constants of air and ground; ω is angular frequency, j is the imaginary unit, σ is the equivalent ground conductivity, ε_r is relative permittivity, and μ_0 and ε_0 are the vacuum permeability and permittivity. Following the ground-parameter setting in Ref. [33], we use $\varepsilon_r = 10$.

$$u_1 = \sqrt{\gamma_1^2 - \gamma_0^2}, \qquad K_1 = \frac{u_1}{\sigma + j\omega\varepsilon_0\varepsilon_r}, \qquad \Delta_{str} = \sqrt{\frac{\varepsilon_0}{\mu_0}}K_1. \tag{10}$$

In Equation (10), u_1 is an auxiliary quantity for calculating surface impedance, K_1 is the ground surface impedance, and Δ_{str} is the normalized surface impedance. Here, K_1 differs from the local station response coefficient K_i in Equation (7). For homogeneous ground, the numerical distance p and Wait frequency-domain attenuation function F_W are

$$p = -\frac{1}{2}\gamma_0 R\Delta_{str}^2, \qquad F_W(p) = 1 - j\sqrt{\pi p}\, e^{-p} erfc\left(j\sqrt{p}\right). \tag{11}$$

In Equation (11), p is the numerical distance, R is propagation distance, $F_W(p)$ is the Wait frequency-domain attenuation function, and erfc is the complementary error function. The magnitude and phase of F_W describe amplitude changes and propagation phase shifts, respectively. Applying this response to the spectrum of the perfectly electrically conducting (PEC) ground reference field from Section 2.1 and taking the inverse Fourier transform yields the propagated waveform.

The numerical frequency band extends to 2 MHz. We use a 180 µs window with 32,768 samples, shift the reference waveform by 30 µs, and apply a cosine taper over 1.8–2.0 MHz. Propagation responses are precomputed at 600 distances from 0.2 to 120 km; τ_E and A_E are linearly interpolated during location. Peak times are estimated by three-point parabolic interpolation around each peak. Comparing the reference and propagated waveforms defines

$$\begin{aligned} \tau_E(R,\sigma) &= t_{peak,\sigma}(R) - t_{peak,PEC}(R) \\ A_E(R,\sigma) &= \frac{\left|E_{peak,\sigma}(R)\right|}{\left|E_{peak,PEC}(R)\right|}. \end{aligned} \tag{12}$$

In Equation (12), τ_E and A_E are the additional peak delay and peak-retention factor. The times $t_{peak,\sigma}$ and $t_{peak,PEC}$ denote the peak arrivals of the finite-conductivity waveform and the PEC reference, respectively; $E_{peak,\sigma}$ and $E_{peak,PEC}$ are the corresponding peak electric fields. The delay enters the TDOA correction in Equation (6), while A_E enters the amplitude recovery in Equation (7). We use $\sigma = 0.010$ S/m for simulations and 0.005 S/m for the rocket-triggered lightning case [35].

2.4. Location and Candidate Discrimination Workflow

Figure 1 summarizes the distinct roles of timing and amplitude in the three-station workflow. Peak arrival times t_i and peak electric fields E_i are extracted from the simulated or measured waveforms, then passed to two branches. The timing branch combines t_i with $\tau_E(R_i)$ for the prescribed ground parameters to generate and retain time-feasible TDOA candidates. The amplitude branch retains E_i and prepares $A_E(R_i)$ and K_i without updating coordinates. The branches meet at candidate scoring: for each fixed candidate, the station distances R_i are calculated, equivalent source-side peaks S_i are recovered, and J_{amp} is evaluated. The candidate with the smaller residual is selected. Although their roles are

separate, amplitude scoring uses distances supplied by the timing branch; these are therefore not two fully independent location algorithms.

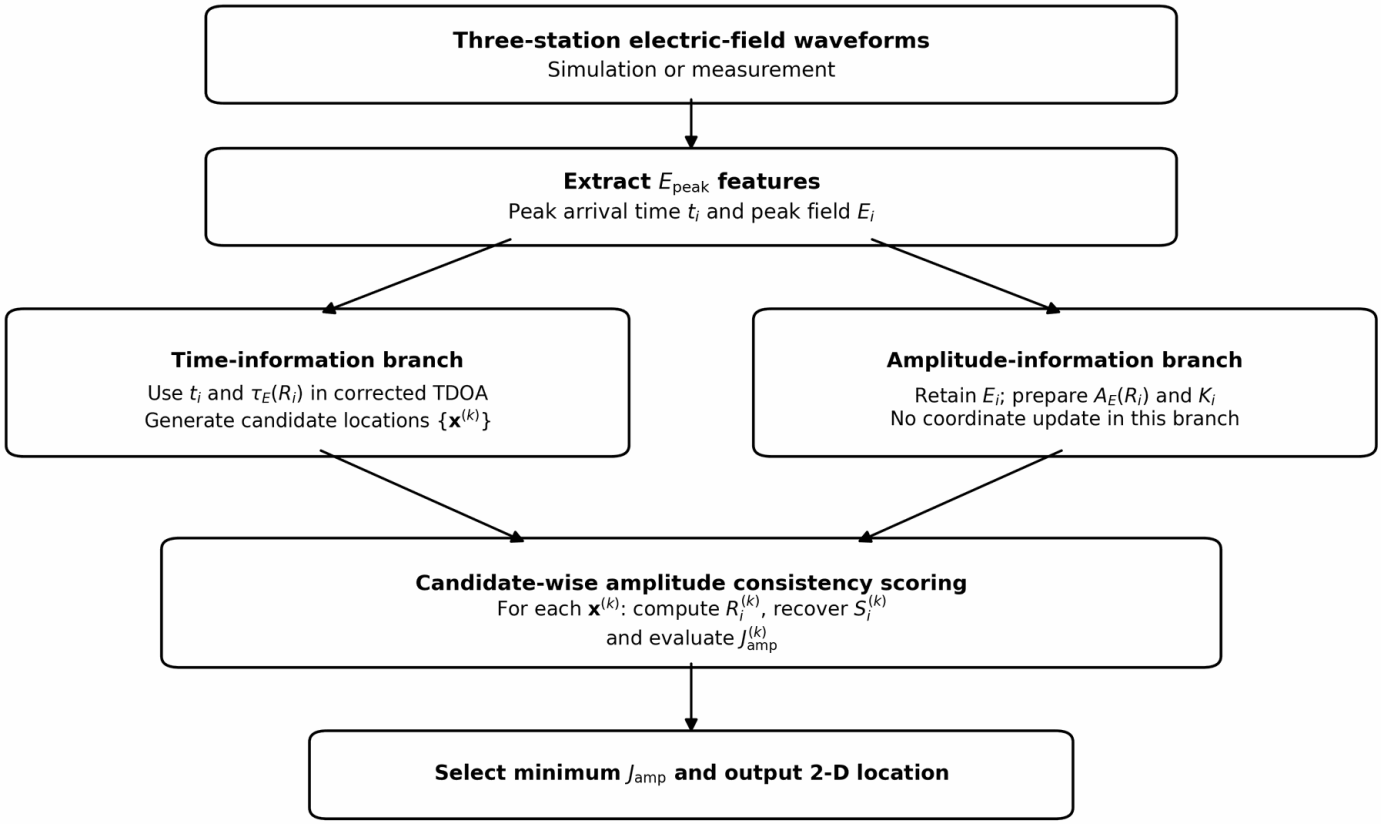


Figure 1. Three-station propagation correction and candidate discrimination. Peak-feature extraction feeds separate timing and amplitude branches. The timing branch generates candidates using τE-corrected TDOA, while the amplitude branch prepares the peak electric fields, AE, and Ki. The branches meet when fixed candidates are scored by Jamp; the output is the two-dimensional location with the smallest peak electric field consistency residual.

3. Results

3.1. Simulation Results

3.1.1. Station Geometry, Finite-Conductivity Propagation, and Peak Generation

This study considers cloud-to-ground return strokes, with rocket-triggered return strokes used for observational validation. Intracloud, intercloud, and other lightning types are outside its scope. The simulated stations are S1 = (−30, 20) km, S2 = (18, 30) km, and S3 = (32, −18) km. The in-network and out-of-network sources are at (2, 8) km and (60, 60) km, respectively. The PEC reference field is generated using a double-Heidler base current, MTLE, and ACM, with $I_{01} = 10.7$ kA, $\tau_{11} = 0.25$ µs, $\tau_{12} = 2.5$ µs, $n_1 = 2$; $I_{02} = 6.5$ kA, $\tau_{21} = 2.1$ µs, $\tau_{22} = 230$ µs, $n_2 = 2$; v = 1.5×10^8 m/s, $\lambda = 2$ km, and H = 7.5 km. Here, I_{01} and I_{02} are the amplitudes of the two Heidler components, τ_{11} and τ_{21} are their front time constants, τ_{12} and τ_{22} are their tail time constants, and n_1 and n_2 control the front shape. Propagation uses $\sigma = 0.010$ S/m and $\varepsilon_r = 10$, with $K_1 = K_2 = K_3 = 1$. The received waveforms in Figures 2–5 include samplewise noise with an RMS level of 0.6% of the peak. The illustrated realization additionally includes 80 ns timing and 1.5% amplitude perturbations. Monte Carlo Set 1 applies 80 ns timing perturbations to compare location errors before and after time correction. Set 2 uses candidates without timing perturbations and applies amplitude perturbations of 1.5%, 5%, 10%, 20%, and 30%. Set 3 combines timing standard deviations of 80 and 160 ns with relative amplitude standard deviations of

5%, 10%, and 20% to test candidate discrimination when both errors are present. The 80 ns level is comparable to the 100 ns sampling interval of the 10 MHz measurements, with sub-sample timing available through peak interpolation. In all three sets, timing generates coordinates and amplitude only ranks candidates. Table 1 lists the main parameters.

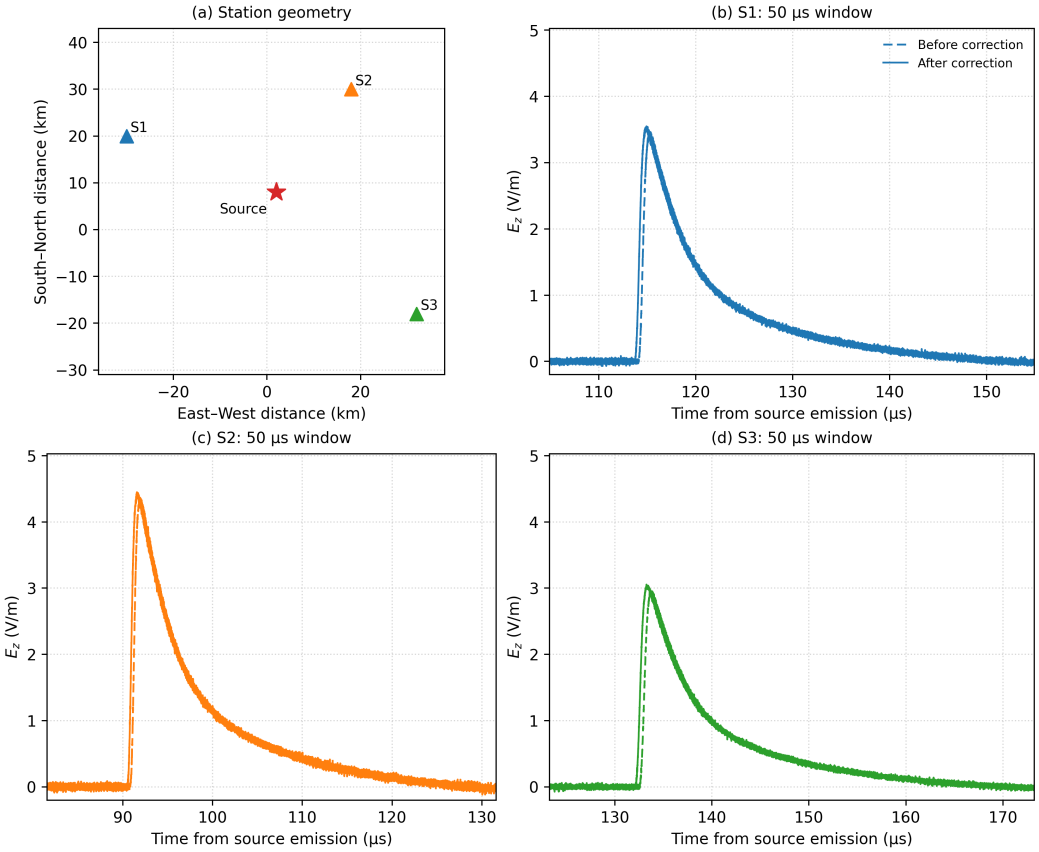


Figure 2. In-network station geometry and received electric fields. (**a**) Station and prescribed source locations; (**b**–**d**) approximately 50 µs waveform windows around the peaks at S1–S3. Dashed lines show finite-conductivity received waveforms with samplewise noise; solid lines show the same noisy waveforms after a $-\tau$E time shift and 1/AE peak-amplitude compensation. All waveform panels share the same V/m scale and retain interstation propagation delays, 1/R amplitude differences, and random noise.

The functions $\tau_{\mathrm{E}}(\mathrm{R})$ and $A_{\mathrm{E}}(\mathrm{R})$ are obtained by comparing unperturbed PEC reference and Wait-propagated waveforms. Figures 2–5 use the same random realization so that the continuous waveforms, extracted peaks, and candidate locations correspond. In the forward calculation, the known distances R_{i} from the prescribed source are used to apply $1/R_{\mathrm{i}}$ geometric attenuation and generate station fields in V/m before adding samplewise noise. These distances are used only to synthesize observations; during inversion, $R_{\mathrm{i}}(\mathrm{x})$ is calculated from each trial location, without using the true source position. The Monte Carlo experiments apply random perturbations directly to peak times and amplitudes: timing only, amplitude only, and both together, as detailed in Sections 3.1.3–3.1.5. For the waveform illustrations, the reference correction applies only a $-\tau_{\mathrm{E}}$ time shift and a $1/A_{\mathrm{E}}$ amplitude rescaling to the same noisy waveform. It does not perform full-band deconvolution or recover a noise-free source waveform. Interstation arrival-time differences, 1/R amplitude differences, and random noise are therefore retained.

Table 1. Main parameters of the three-station simulations.

Parameter	Value	Purpose
Station coordinates S1/S2/S3	$(-30, 20)/(18, 30)/(32, -18)$ km	Three-station network
Propagation band	0–2 MHz; cosine taper over 1.8–2.0 MHz	Wait frequency-domain calculation
Source locations In-network/out-of-network	$(2, 8)/(60, 60)$ km	Two location scenarios
Equivalent conductivity σ	0.010 S/m	Wait propagation input
Reference electric field	Double-Heidler base current; MTLE; ACM; v = 1.5×10^8 m/s; $\lambda = 2$ km; H = 7.5 km	PEC reference waveform
Local station response K_i	1/1/1	No interstation enhancement differences
Samplewise noise Illustrated waveforms	RMS = 0.6% of received peak	Noise in forward waveforms
Peak-time perturbation	SD = 80 ns; also 160 ns in Set 3	Sets 1 and 3; illustrated realization
Peak-amplitude perturbation	1.5% (illustration); 1.5%, 5%, 10%, 20%, 30% (Set 2); 5%, 10%, 20% (Set 3)	Sets 2 and 3; illustrated realization
Monte Carlo trials	500 per condition and scenario	Sets 1, 2, and 3

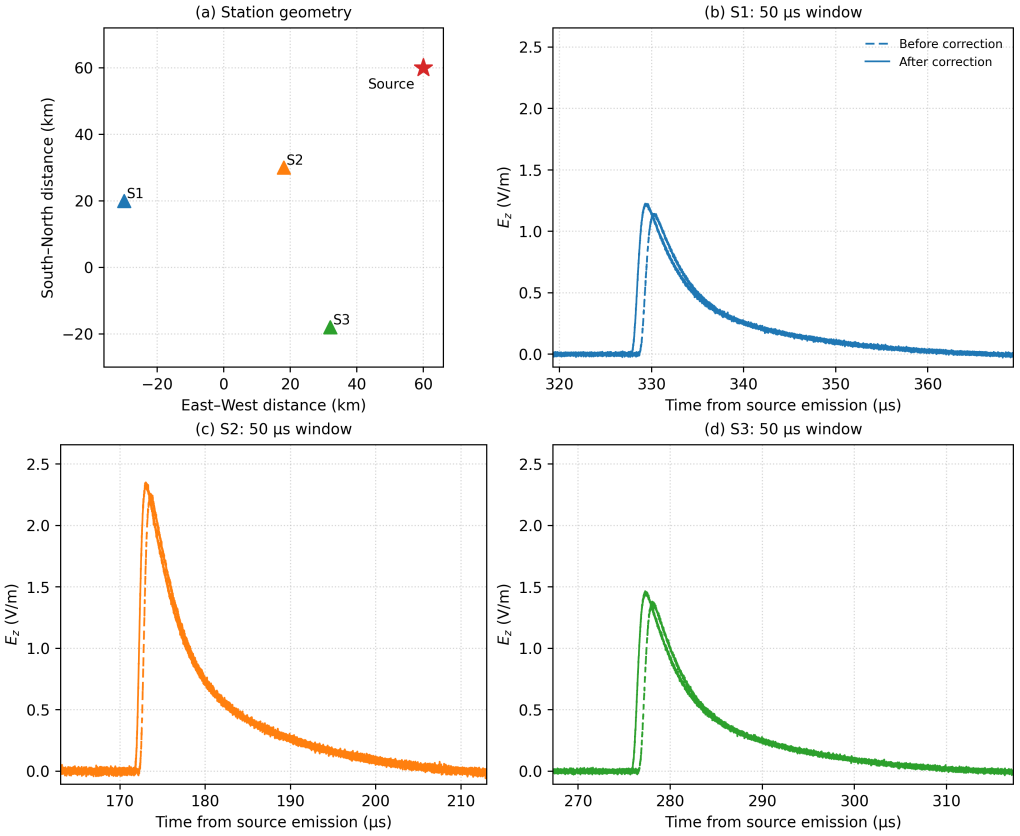


Figure 3. Out-of-network station geometry and received electric fields. (**a**) Station and prescribed source locations; (**b**–**d**) approximately 50 μs waveform windows around the peaks at S1–S3. Dashed lines show finite-conductivity received waveforms with samplewise noise; solid lines show the same noisy waveforms after a $-\tau$E time shift and 1/AE peak-amplitude compensation. All waveform panels share the same V/m scale and retain interstation propagation delays, 1/R amplitude differences, and random noise.

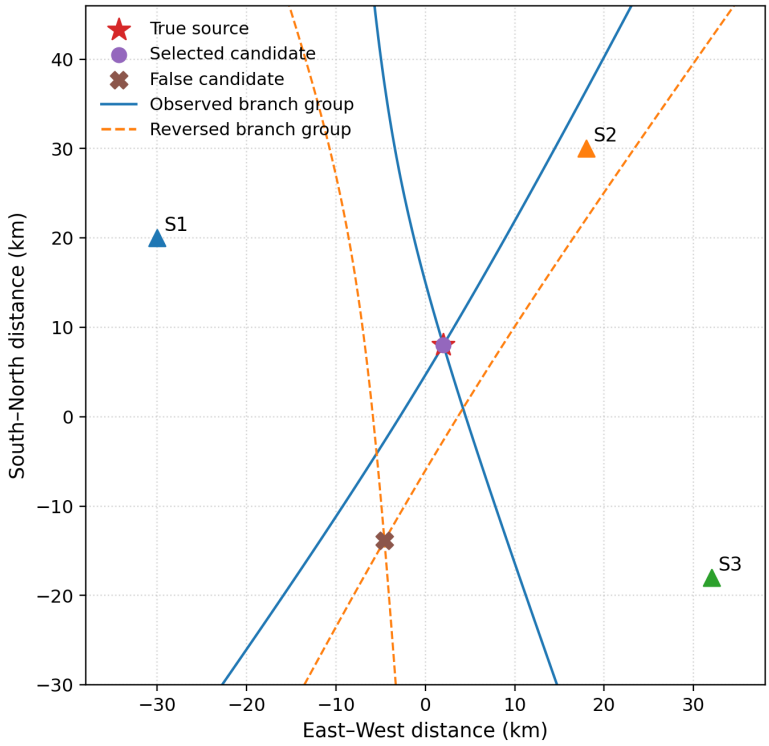


Figure 4. Controlled in-network spurious candidate and ACM discrimination. With S1 as the reference, solid blue curves are the τE-corrected S1–S2 and S1–S3 TDOA constraints for g = +1; dashed orange curves are the corresponding constraints after jointly reversing their signs with g = −1. Intersections between curves of the same line style form candidates; mixed-style intersections are excluded. Once coordinates are fixed, candidate distances determine AE and, together with station responses, recover source-side peaks for Jamp ranking. Triangles mark stations, the red star the prescribed source, the purple dot the selected candidate with lower Jamp, and the brown cross the rejected spurious candidate.

3.1.2. In-Network and Out-of-Network Candidate Discrimination

The in-network and out-of-network tests use different ways of generating candidates but apply the same peak-consistency criterion. In Figure 4, g = +1 produces the correct in-network candidate and g = −1 produces a controlled spurious candidate. For this random realization, time correction reduces the location error from 46.0 to 21.8 m, and the two J_{amp} values are 0.00102 and 0.263. In Figure 5, the out-of-network scenario uses only g = +1; the same constraint set produces both the correct and spurious candidates. The error decreases from 1867.3 to 394.8 m, with J_{amp} values of 0.00088 and 0.518. In both cases, TDOA and τ_{E} determine coordinates, and J_{amp} ranks candidates only after the coordinates are fixed. Amplitude information therefore does not alter the timing-based locations.

3.1.3. Location Accuracy Under Timing Perturbations

Monte Carlo Set 1 evaluates only the effect of propagation-time correction on location accuracy. For each scenario, 500 paired trials add random perturbations with a standard deviation of 80 ns to the three peak arrival times. Exactly the same perturbations are used before and after correction. The timing branch solves for coordinates with and without τ_{E}, and the resulting location errors are compared. Table 2 reports the 10th–90th percentile interval (P10–P90), which contains the middle 80% of trial errors.

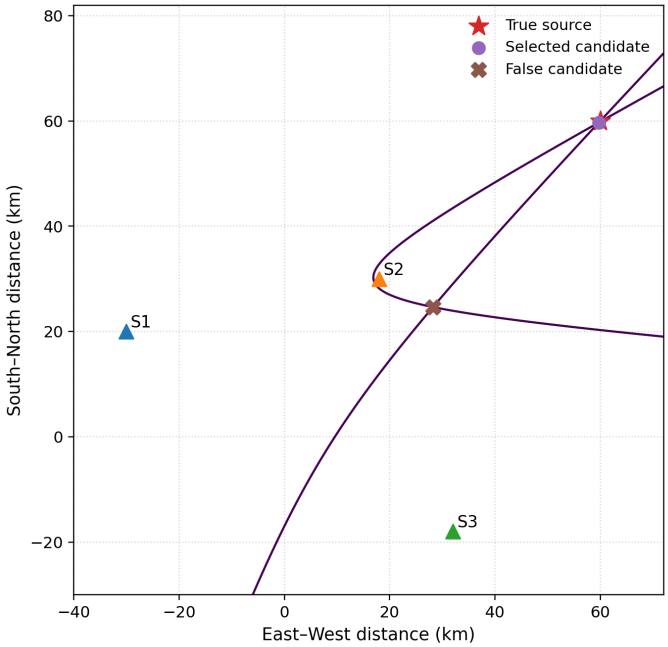


Figure 5. Two out-of-network candidates from the original signed TDOA constraints and their ACM discrimination. With S1 as the reference, the two purple curves are the τE-corrected S1–S2 and S1–S3 constraints. Both intersections are retained as time-feasible candidates. Once coordinates are fixed, candidate distances determine AE and, together with station responses, recover source-side peaks for Jamp ranking. Triangles mark stations, the red star the prescribed source, the purple dot the selected candidate with lower Jamp, and the brown cross the rejected spurious candidate.

Table 2. Location errors in 500 paired Monte Carlo trials with and without propagation-time correction.

Scenario	Uncorrected Error P10–P90 (m)	Corrected Error P10–P90 (m)
In-network	12.8–59.7	9.8–46.2
Out-of-network	870.6–2130.5	75.4–808.0

3.1.4. ACM Candidate Selection Under Amplitude Perturbations

Monte Carlo Set 2 evaluates the effect of amplitude perturbations on ACM candidate discrimination. Propagation-corrected candidates are first generated from peak times without timing perturbations, and their coordinates remain fixed across all five amplitude levels. Each scenario uses 500 trials, with the same standardized random samples scaled to relative amplitude perturbations of 1.5%, 5%, 10%, 20%, and 30%. The paired ablation with and without A_{E} uses identical coordinates and amplitude perturbations. The full method uses the candidate-specific A_{E} in Equation (7); the comparison sets only $A_{\mathrm{E}} = 1$, leaving K_{i}, the J_{amp} formula, and all other parameters unchanged. The in-network test compares the correct $\mathrm{g} = +1$ candidate with the controlled $\mathrm{g} = -1$ spurious candidate, while the out-of-network test compares the two $\mathrm{g} = +1$ candidates. A selection is correct when the correct candidate has the smaller J_{amp}.

To quantify how A_{E} affects candidate separation, we define the residual difference $\Delta J_{\mathrm{amp}} = J_{\mathrm{amp,spurious}} - J_{\mathrm{amp,correct}}$. A positive value indicates correct selection, whereas a negative value indicates selection of the spurious candidate. Table 3 reports its median over 500 trials. Including A_{E} slightly increases the median difference in the in-network scenario, indicating improved separation. The increase is larger outside the network and improves the correct-selection rate at higher amplitude perturbation levels.

Table 3. Correct-selection rates and median candidate-residual differences under relative peak-amplitude perturbations (500 trials per scenario). Paired values are without AE/with AE compensation.

Amplitude SD (%)	In-Network		Out-of-Network	
	Correct Selection (%)	Median ΔJ_{amp}	Correct Selection (%)	Median ΔJ_{amp}
1.5	100.0/100.0	0.234/0.241	100.0/100.0	0.525/0.565
5	100.0/100.0	0.234/0.242	100.0/100.0	0.526/0.565
10	99.4/99.4	0.236/0.243	100.0/100.0	0.526/0.565
20	87.4/87.4	0.239/0.246	95.4/96.2	0.518/0.558
30	79.4/79.4	0.243/0.251	84.0/86.2	0.504/0.543

3.1.5. ACM Candidate Selection Under Joint Timing and Amplitude Perturbations

Monte Carlo Set 3 considers timing and amplitude errors simultaneously. Timing standard deviations of 80 and 160 ns are combined with relative amplitude standard deviations of 5%, 10%, and 20%, with 500 trials for each combination and scenario. In each trial, Gaussian timing and amplitude perturbations are generated independently and applied together to the three peak times and amplitudes. The perturbed times generate propagation-corrected TDOA candidates, and the perturbed amplitudes determine J_{amp}. Coordinates are recalculated for each timing realization. All six combinations use the same standardized random samples, scaled by their respective standard deviations; the three amplitude levels at a given timing level share candidate coordinates. Sets 2 and 3 reuse amplitude samples at matching amplitude levels. Scoring with and without A_E uses identical noisy observations and candidates.

Table 4 summarizes the six joint-perturbation conditions. With A_E compensation, 80 ns timing and 5% amplitude perturbations give 100% correct selection in both scenarios. The median ΔJ_{amp} values are 0.242 and 0.565, and the minimum values are 0.102 and 0.325 for the in-network and out-of-network scenarios, respectively, indicating separation of the candidates in every trial. At 20% amplitude perturbation, the correct-selection rates are 87.4% inside the network and 96.2% outside it at both timing levels. Within the tested conditions, increasing the timing standard deviation from 80 to 160 ns has little effect on the selection rate or median ΔJ_{amp}, whereas larger amplitude perturbations reduce the correct-selection rate.

Table 4. Correct-selection rates and median ΔJamp under six combinations of timing and amplitude perturbations (500 trials per combination and scenario). Paired values are without AE/with AE compensation.

Timing SD (ns)	Amplitude SD (%)	In-Network		Out-of-Network	
		Correct Selection (%)	Median ΔJ_{amp}	Correct Selection (%)	Median ΔJ_{amp}
80	5	100.0/100.0	0.234/0.242	100.0/100.0	0.525/0.565
80	10	99.4/99.4	0.235/0.243	100.0/100.0	0.525/0.565
80	20	87.4/87.4	0.239/0.247	95.4/96.2	0.520/0.559
160	5	100.0/100.0	0.235/0.242	100.0/100.0	0.526/0.566
160	10	99.4/99.2	0.236/0.243	100.0/100.0	0.524/0.564
160	20	87.4/87.4	0.239/0.247	95.4/96.2	0.522/0.561

3.2. Validation with Rocket-Triggered Lightning

3.2.1. Data, Three-Station Geometry, and Propagation Environment

The measured case is the second return stroke of a rocket-triggered flash recorded during the Guangdong Comprehensive Observation Experiment on Lightning Discharge at 18:22 Beijing time on 11 June 2015. Each .fig file in the archive supplied by the experimental

team contains a 1 ms digitized waveform with 10,000 samples (10 MHz). Accompanying text files provide return-stroke sample indices, absolute peak times, precise station coordinates, and the triggering location. The original .fig YData arrays contain digitizer counts, without a complete set of station-specific conversion factors from ADC counts to V/m. Stations S7, S8, and S9 correspond to XTC, TMZ, and ZCJ, at (113.680980°E, 23.559921°N), (113.289740°E, 23.547201°N), and (113.820678°E, 23.298667°N), respectively. The triggering point is at (113.5953°E, 23.6389°N). The location is performed in a WGS84 azimuthal equidistant projection centered on the station network. After inversion, the triggering point is transformed into the same coordinate system for error evaluation. For display only, Figures 6–8 translate all coordinates so that the triggering point is the origin.

Table 5 lists station distances, absolute peak times, peak electric fields, and local responses; the geometry follows Zhang et al. [35]. Figure 6a shows the relative station geometry. Waveform shapes and sampling times in Figure 6b–d are read directly from the original .fig arrays. To match the processing bandwidth used by Zhang et al. [35] for Case 2, we remove the pre-pulse baseline and apply a fourth-order zero-phase Butterworth low-pass filter with a 2 MHz cutoff before plotting. Because the original arrays lack complete ADC-to-V/m calibration factors, each waveform is scaled at a single point to the corresponding S7, S8, or S9 peak field reported for Case 2, without using the triggering location or the locations estimated here. All three panels use the S7 peak as time zero, but each displays only the interval from 10 μs before to 45 μs after its own peak. The red peak markers therefore remain at approximately 0, 68.684, and 106.774 μs, preserving the measured interstation time differences. Absolute peak times are taken from Table 5. This plotting procedure does not change the location or ACM inputs. The measured case uses $\sigma = 0.005$ S/m, $\varepsilon_r = 10$, and a 2 MHz propagation bandwidth. The simulated conductivity, 0.010 S/m, is one of the standard representative values in the ITU-R P.832-4 ground-conductivity classification [36,37]. It serves as a uniform-ground benchmark for testing location and discrimination under known propagation conditions. The measured value, 0.005 S/m, follows Zhang et al. [35,38], who describe it as typical of dry soil at the Guangdong experimental site. Thus, the simulation uses a standard reference value and the measured case uses a site-specific literature value; they do not use the same conductivity. The method is not restricted to either value. In practice, equivalent conductivity can be obtained from regional measurements or conductivity maps suitable for the frequency band, after which τ_E and A_E are recalculated. We do not infer or optimize conductivity using the triggering location. Its influence is tested in Section 3.3.

Table 5. Peak observations and local response parameters for the S7–S8–S9 rocket-triggered lightning case.

Station	Distance to Source (km)	Absolute Peak Time (s)	Peak Field (V/m)	Local Enhancement K_i
S7	12.369	51.750245386	24.5	1.82
S8	32.800	51.750314070	5.5	1.44
S9	44.159	51.750352160	4.6	1.62

For this case, K_i in Equation (7) is taken from the building-related local peak-field enhancement factors in Table 1 of Zhang et al. [35]: 1.82, 1.44, and 1.62 for S7, S8, and S9, respectively. That study used the measured channel-base current as input and fitted the electric field at Station No. 1 to determine channel-model parameters. It defined local enhancement as the ratio of the rooftop peak field to the ground-reference peak field and applied the same estimation approach to Case 2. These K_i values are therefore site-response estimates derived from comparisons of return-stroke observations and modeling. They are

neither instrument coefficients calibrated independently of lightning data nor ADC-to-V/m conversion factors. Here, they are fixed inputs shared by all candidates and are not refitted or adjusted using candidate positions or J_{amp}.

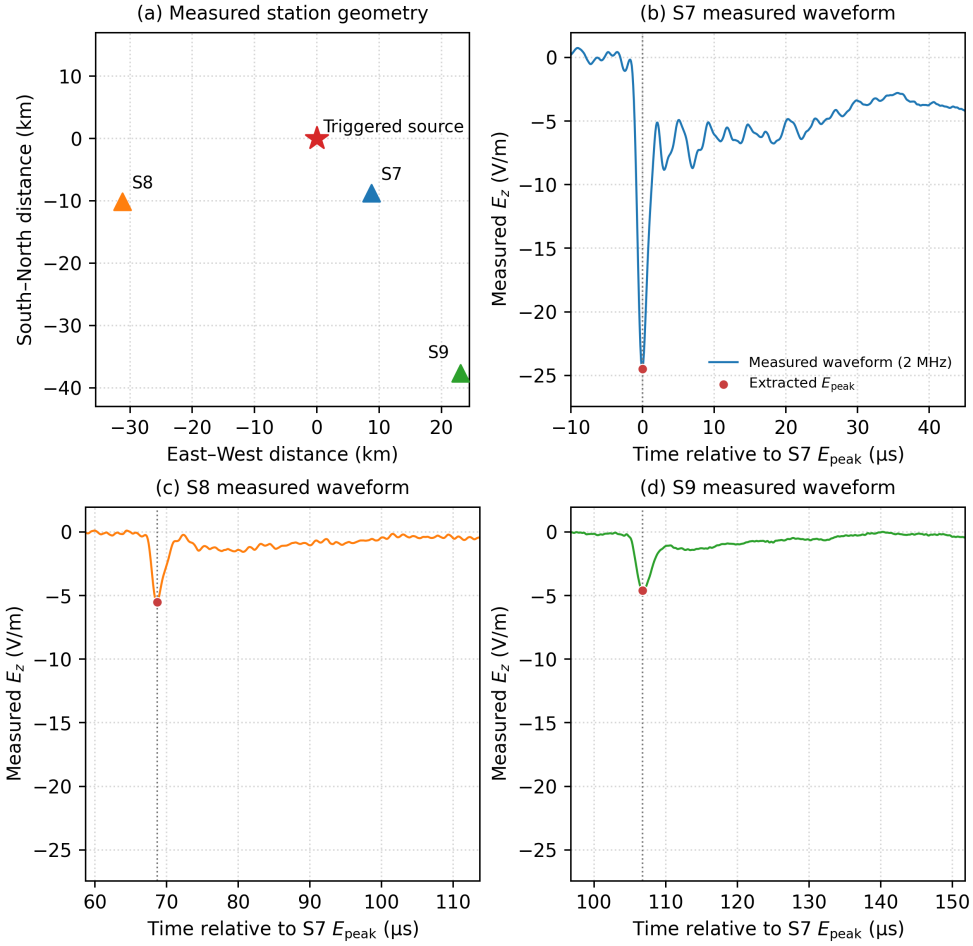


Figure 6. S7–S8–S9 geometry and measured electric fields for the rocket-triggered lightning case. (**a**) Relative station geometry; (**b**–**d**) waveforms read from the original .fig arrays, with pre-pulse baseline removal and 2 MHz zero-phase low-pass filtering, then scaled to V/m using the corresponding measured peaks reported by Zhang et al. [35] for Case 2. All waveform panels share the same vertical scale and S7 peak-time reference. Each shows only the interval from 10 μs before to 45 μs after its own peak. The red markers retain the measured interstation peak-time differences.

3.2.2. Conductivity-Based Peak-Time Correction and Candidate Generation

The timing branch uses only the original S7–S8–S9 peak times, precise station coordinates, the prescribed $\sigma = 0.005$ S/m propagation environment, and the g = +1 branch consistent with the observed arrival order. For each trial location x, distances $R_i(x)$ are calculated and the corresponding $\tau_E[R_i(x),\sigma]$ values are combined with geometric travel times in the TDOA residual. Candidate coordinates use no amplitude information, and propagation coefficients are not calibrated against the true triggering position. As a reference for the delay magnitude, the model gives additional delays of 0.295, 0.653, and 0.801 μs for S7, S8, and S9 at the true source-to-station distances listed in Table 5.

The two uncorrected candidates are 1.333 and 11.198 km from the triggering point. After time correction with $\sigma = 0.005$ S/m, the respective errors are 0.360 and 12.798 km. Coordinates are generated exclusively by the propagation-corrected TDOA timing branch. The amplitude branch in Section 3.2.3 calculates J_{amp} only after the candidates are fixed; it does not participate in coordinate estimation.

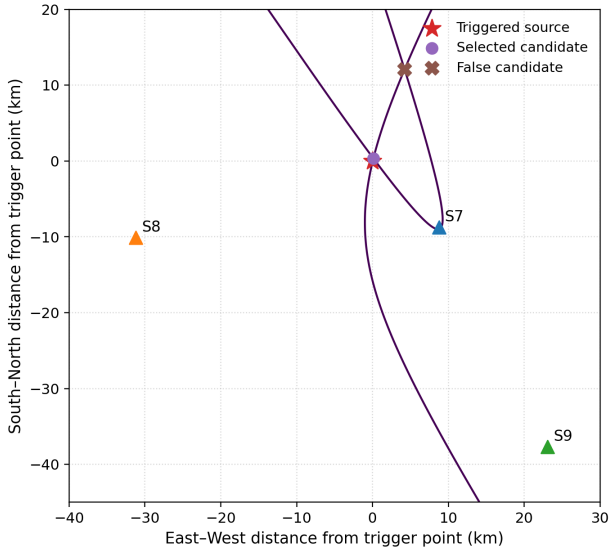


Figure 7. TDOA candidates and ACM discrimination for the S7–S8–S9 rocket-triggered lightning case. With S7 as the reference, the purple curves are the τE-corrected S7–S8 and S7–S9 constraints for g = +1. Both intersections are retained as time-feasible candidates. Candidate distances determine AE and, together with station responses, recover source-side peaks for Jamp ranking. Triangles mark stations, the red star the triggering point, the purple dot the selected candidate with lower Jamp, and the brown cross the rejected spurious candidate. Coordinates are translated so that the triggering point is the origin.

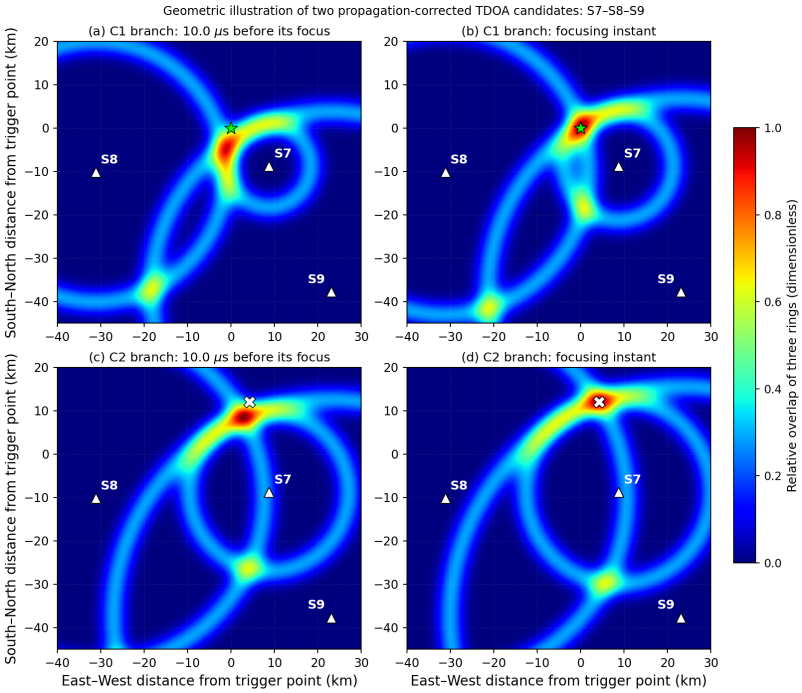


Figure 8. Geometric back-propagation for two propagation-corrected S7–S8–S9 TDOA candidates. Colored annuli are centered on the stations, with radii determined by travel time. All panels share a dimensionless 0–1 scale; blue to red indicates increasing relative overlap of the three annuli. Axes show east–west and south–north distances from the triggering point in kilometers. White triangles mark stations, the green star the triggering point, and the white cross Candidate 2. Each row uses its own candidate time reference: (**a**,**b**) Candidate 1 at 10.0 µs before convergence and at convergence; (**c**,**d**) the corresponding instants for Candidate 2. This is a geometric illustration of timing constraints, not a complete electromagnetic wavefield.

Figure 8 illustrates the travel-time geometry of the two time-feasible candidates by geometric back-propagation. For each fixed candidate from Equation (6), the travel time $R_i/c + \tau_E(R_i,\sigma)$ is subtracted from each observed peak time. The average over the three stations defines that candidate's source-side peak time. Using this time as the reference and the travel-time–distance relationship from Section 2.3, circle radii are calculated and circles are drawn around the stations. The upper and lower rows use their respective candidate time references and show 10.0 μs before convergence and the convergence instant. Gaussian annuli visualize the circles; color shows their dimensionless relative overlap. No full-waveform time reversal or electromagnetic wavefield solution is performed. Color represents neither field strength nor energy. Convergence only shows that a candidate satisfies the corrected timing constraints; it is not independent evidence of a correct location and is not used in candidate estimation or scoring. Candidate selection remains based on ACM peak electric field consistency.

3.2.3. Amplitude Compensation and ACM Candidate Discrimination

The amplitude branch is applied after the coordinates are fixed. S7, S8, and S9 peak electric field magnitudes are taken from the measured waveforms in V/m reported by Zhang et al. [35] for Case 2, and local building enhancement factors are taken from their Table 1. The values are listed in Table 5. For each candidate k, distances $R_i^{(k)}$ are calculated and the precomputed distance-dependent peak attenuation gives $A_E(R_i^{(k)},0.005)$ for each path. Equation (7) then compensates for local response and finite-conductivity attenuation, recovers equivalent source-side peaks at the three stations, and permits the candidates to be compared using peak electric field consistency.

After compensation for distance, local response, and propagation attenuation, Candidate 1 yields more consistent source-side peaks. The two J_{amp} values are 0.0419 and 0.2238, respectively, so the ACM selects Candidate 1 (Table 6).

Table 6. S7–S8–S9 candidate locations before and after ACM–Wait propagation correction, and ACM selection results.

Candidate	Propagation Correction	Distance to Source (km)	J_{amp}	ACM Selection
1	None	1.333	—	—
2	None	11.198	—	—
1	$\sigma = 0.005$ S/m	0.360	0.0419	Selected
2	$\sigma = 0.005$ S/m	12.798	0.2238	Rejected

3.3. Sensitivity to Ground Conductivity

To assess the influence of conductivity on location and candidate selection, the correction-model σ is varied over 0.002, 0.005, 0.010, 0.015, and 0.020 S/m, with $\varepsilon_r = 10$ and the original bandwidth unchanged. Inputs are the two simulated observation sets used for the individual examples in Section 3.1 and the measured observations from Section 3.2. Peak times, peak amplitudes, and K_i remain fixed. The simulated observations were generated at $\sigma = 0.010$ S/m and are not regenerated for each test conductivity. For each σ, τ_E and A_E are recalculated, candidates are obtained from timing, and J_{amp} ranks them. Candidate generation follows the earlier procedure, including the controlled conjugate spurious candidate for the in-network scenario. Known source locations are used only to calculate errors and identify the correct candidates.

In Table 7, error is the distance between the ACM-selected candidate and the known source, and ΔJ_{amp} follows Section 3.1.4. All three cases have positive ΔJ_{amp} at every tested conductivity, so candidate selection does not reverse. Location errors nevertheless vary

with σ: the measured-case error ranges from 59.4 to 1038.0 m. Stable candidate selection therefore does not imply conductivity-independent location accuracy. Smaller errors at some nonbaseline values may reflect cancellation between propagation-parameter and observation errors; they do not establish the true site conductivity. We retain the original baseline values. These results concern two fixed simulated observation sets and one measured event, not a statistical success rate across events.

Table 7. Location errors and candidate-residual differences for different correction-model conductivities with fixed observations ($\varepsilon r = 10$).

σ (S/m)	In-Network		Out-of-Network		Measured Case	
	Error (m)	ΔJ_{amp}	Error (m)	ΔJ_{amp}	Error (m)	ΔJ_{amp}
0.002	12.3	0.2720	1003.9	0.6002	59.4	0.1884
0.005	7.1	0.2657	124.2	0.5506	359.9	0.1819
0.010	21.8	0.2623	394.8	0.5176	731.5	0.1725
0.015	29.3	0.2599	667.2	0.5004	924.4	0.1682
0.020	33.5	0.2581	928.3	0.4913	1038.0	0.1660

4. Discussion

4.1. Roles of Simulations and Observational Validation

The simulations use the same ACM–MTLE–Wait model to generate observations and correction quantities. The three Monte Carlo sets serve distinct purposes. Set 1 compares location errors before and after time correction under timing perturbations. Set 2 uses candidates without timing perturbations and compares selection with and without A_E at different amplitude levels. Set 3 combines 80 and 160 ns timing perturbations with 5%, 10%, and 20% amplitude perturbations to evaluate selection when both errors are present. Sets 2 and 3 share amplitude samples at matching levels to compare results with and without timing errors. All before/after and with/without-A_E comparisons use the same observation perturbations. These simulations test the internal consistency and numerical stability of the workflow. Because the forward and correction calculations share a propagation model, however, the reduction in timing error is not independent evidence of real-world propagation accuracy.

The rocket-triggered lightning data provide complementary external validation. Neither the measured peak times nor the published peak electric fields are fitted to the propagation corrections using the true triggering position. The conductivity of 0.005 S/m is prescribed in advance, and the triggering coordinates are used only for error evaluation after inversion. In both the simulations and measured case, timing generates coordinates and amplitude ranks peak consistency only after the candidates are fixed.

4.2. Separate Roles of Time Correction and ACM Peak Consistency

The roles of τ_E and A_E are distinct. The delay enters the TDOA range-difference constraints and changes candidate coordinates; A_E leaves coordinates unchanged and affects J_{amp} through source-side peak recovery. The Wait surface impedance and attenuation function generate these two responses for specified conductivity, permittivity, bandwidth, and distance. Paired comparisons show that A_E increases the candidate-residual difference in both scenarios. The increase is modest inside the network and larger outside it, where A_E also improves correct selection at higher amplitude perturbations. This difference may reflect propagation paths, network geometry, and candidate distributions, as well as perturbation levels; the present tests do not isolate a single cause. The conductivity used here is an equivalent uniform value for a region or path, not a complete retrieval

of a heterogeneous surface. The interpretation of τ_E and A_E is therefore limited to the prescribed ground parameters and applicable band. The Wait approximation is not treated as a complete propagation model for complex paths.

4.3. Physical Significance of the Three-Station Measured Case

S7–S8–S9 provides the minimum three-station configuration for two-dimensional TDOA and yields two spatially separated candidates under the same g = +1 constraints. This case tests two distinct questions: whether τ_E reduces the geometric bias of the correct candidate under a known propagation environment, and whether the same three peak fields provide an additional physical criterion between two time-feasible locations. After correction, Candidate 1 lies closer to the triggering point and gives less dispersed recovered source-side peaks and a lower J_{amp}. Amplitude information can therefore help reject a time-feasible candidate with weaker physical consistency.

4.4. Limitations and Future Work

Four main limitations apply. First, propagation correction uses a single equivalent conductivity and does not represent heterogeneous surfaces or complex terrain along the three paths. Second, the Wait attenuation function primarily applies to propagation over finitely conducting ground where radiation dominates [32]. With ε_r fixed at 10 and bandwidth limited to 2 MHz, applications across frequency bands, in the near field, or along complex paths require renewed validation. Third, the ACM reference assumes a straight vertical channel, constant return-stroke speed, and exponential MTLE attenuation to obtain far-field peak characteristics; realistic three-dimensional channel tortuosity is not included. Fourth, the original .fig waveforms lack a complete set of station-specific ADC-to-V/m conversion factors. Figure 6 uses waveform shapes and timing from the original arrays, with traceable single-point amplitude scaling to the peaks reported by Zhang et al. [35] for Case 2. Measured amplitude discrimination therefore depends on the published V/m peaks and local response coefficients, without independent absolute-amplitude recalibration of the observation system. Section 3.3 tests only uniform conductivity changes, not permittivity uncertainty or its interaction with conductivity. Fixing $\varepsilon_r = 10$ is thus a condition of the analysis, not evidence that permittivity effects are negligible. Spatially heterogeneous or frequency-dependent ground properties may still bias τ_E and A_E and affect location errors and J_{amp} ranking.

The joint-perturbation experiments include both peak-time and peak-amplitude errors, but generate them as separate Gaussian random variables. They do not model the correlated errors that may arise when both features are extracted from the same noisy waveform. The results assess candidate discrimination under simultaneous independent errors and cannot establish robustness to correlated errors or actual receiver noise.

The minimum three-station two-dimensional TDOA configuration targets sparse networks with limited installation and maintenance budgets. The aim is to improve accuracy through propagation-time correction and discriminate spurious candidates through ACM amplitude consistency without adding stations. Additional stations provide redundant observations that, together with least-squares adjustment and residual tests, can further improve accuracy and identify station-specific gross errors. They also increase deployment, synchronization, and maintenance costs. The performance of the proposed method in larger networks remains to be evaluated.

Future work could use soil-moisture, land-cover, and other remote-sensing products to characterize surface differences along individual paths and develop spatially heterogeneous propagation corrections. Larger samples of rocket-triggered and natural lightning would help assess the stability of τ_E and A_E across waveforms and propagation conditions.

The reference field could also be extended to more realistic three-dimensional channels, including inclined and tortuous geometries.

5. Conclusions

We propose a propagation-correction and candidate-discrimination method for sparse three-station VLF/LF lightning location, using peak-time correction to improve candidate positions and ACM peak electric field consistency to select among them. In the S7–S8–S9 rocket-triggered lightning case, time correction with prescribed ground parameters reduces the near-candidate error from 1.333 to 0.360 km, after which the ACM criterion selects that candidate and rejects the spurious solution. The results show that time correction and ACM consistency respectively support lower location error and rejection of spurious candidates without additional stations; because performance may depend on network geometry and terrain, validation across different baselines and layout orientations is still needed to establish the range of applicability.

Author Contributions: Conceptualization, Y.X. and Y.Z.; methodology, Y.X. and Y.Z.; software, Y.X.; validation, Y.X. and B.W.; formal analysis, Y.X.; investigation, Y.X.; resources, Y.Z.; data curation, Y.X. and B.W.; writing—original draft preparation, Y.X.; writing—review and editing, Y.X. and Y.Z.; visualization, Y.X.; supervision, Y.Z.; project administration, Y.Z.; funding acquisition, Y.Z. All authors have read and agreed to the published version of the manuscript.

Funding: This research was funded by the National Natural Science Foundation of China, grant number 42005065.

Institutional Review Board Statement: Not applicable.

Informed Consent Statement: Not applicable.

Data Availability Statement: Restrictions apply to the availability of these data. The multistation waveform and timing data were obtained from the GCOELD/LFEDA experimental team associated with Zhang et al. [35] and are available from the corresponding author with the permission of the data provider.

Acknowledgments: The authors sincerely thank Mingli Chen and the GCOELD/LFEDA experimental team for providing the original multistation waveforms and timing data used in the rocket-triggered lightning validation. During the preparation of this manuscript, the authors used ChatGPT (GPT-6 Astra, OpenAI) for English-language polishing, readability improvement, grammar checking, and formatting refinement. The authors reviewed and take responsibility for the final content.

Conflicts of Interest: The authors declare no conflicts of interest.

Abbreviations

The following abbreviations and peak-field notation are used in this manuscript:

ACM	Accelerating charge method
TDOA	Time difference of arrival
VLF	Very low frequency
LF	Low frequency
Epeak	Peak electric field feature

References

1. Cummins, K.L.; Murphy, M.J. An Overview of Lightning Locating Systems: History, Techniques, and Data Uses, with an In-Depth Look at the U.S. National Lightning Detection Network. *IEEE Trans. Electromagn. Compat.* **2009**, *51*, 499–518. [CrossRef]
2. Nag, A.; Murphy, M.J.; Schulz, W.; Cummins, K.L. Lightning Locating Systems: Insights on Characteristics and Validation Techniques. *Earth Space Sci.* **2015**, *2*, 65–93. [CrossRef]
3. Cummins, K.L.; Murphy, M.J.; Bardo, E.A.; Hiscox, W.L.; Pyle, R.B.; Pifer, A.E. A Combined TOA/MDF Technology Upgrade of the U.S. National Lightning Detection Network. *J. Geophys. Res. Atmos.* **1998**, *103*, 9035–9044. [CrossRef]

4. Shi, D.; Zheng, D.; Zhang, Y.; Zhang, Y.; Huang, Z.; Lu, W.; Chen, S.; Yan, X. Low-Frequency E-Field Detection Array (LFEDA)-Construction and Preliminary Results. *Sci. China Earth Sci.* **2017**, *60*, 1896–1908. [CrossRef]
5. Wang, Y.; Qie, X.; Wang, D.; Liu, M.; Su, D.; Wang, Z.; Liu, D.; Wu, Z.; Sun, Z.; Tian, Y. Beijing Lightning Network (BLNET) and the Observation on Preliminary Breakdown Processes. *Atmos. Res.* **2016**, *171*, 121–132. [CrossRef]
6. Chan, Y.T.; Ho, K.C. A Simple and Efficient Estimator for Hyperbolic Location. *IEEE Trans. Signal Process.* **1994**, *42*, 1905–1915. [CrossRef]
7. Koshak, W.J.; Solakiewicz, R.J.; Blakeslee, R.J.; Goodman, S.J.; Christian, H.J.; Hall, J.M.; Bailey, J.C.; Krider, E.P.; Bateman, M.G.; Boccippio, D.J.; et al. North Alabama Lightning Mapping Array (LMA): VHF Source Retrieval Algorithm and Error Analyses. *J. Atmos. Ocean. Technol.* **2004**, *21*, 543–558. [CrossRef]
8. Lyu, F.; Cummer, S.A.; Solanki, R.; Weinert, J.; McTague, L.; Katko, A.; Barrett, J.; Zigoneanu, L.; Xie, Y.; Wang, W. A Low-Frequency Near-Field Interferometric-TOA 3-D Lightning Mapping Array. *Geophys. Res. Lett.* **2014**, *41*, 7777–7784. [CrossRef]
9. Cooray, V. Effects of Propagation on the Return Stroke Radiation Fields. *Radio Sci.* **1987**, *22*, 757–768. [CrossRef]
10. Honma, N.; Suzuki, F.; Miyake, Y.; Ishii, M.; Hidayat, S. Propagation Effect on Field Waveforms in Relation to Time-of-Arrival Technique in Lightning Location. *J. Geophys. Res. Atmos.* **1998**, *103*, 14141–14145. [CrossRef]
11. Cooray, V.; Fernando, M.; Sorensen, T.; Gotschl, T.; Pedersen, A. Propagation of Lightning Generated Transient Electromagnetic Fields over Finitely Conducting Ground. *J. Atmos. Sol.-Terr. Phys.* **2000**, *62*, 583–600. [CrossRef]
12. Schueler, J.R.; Thomson, E.M. Estimating Ground Conductivity and Improving Lightning Location Goodness of Fit by Compensating Propagation Effects. *Radio Sci.* **2006**, *41*, RS1001. [CrossRef]
13. Li, D.; Azadifar, M.; Rachidi, F.; Rubinstein, M.; Diendorfer, G.; Sheshyekani, K.; Zhang, Q.; Wang, Z. Analysis of Lightning Electromagnetic Field Propagation in Mountainous Terrain and Its Effects on ToA-Based Lightning Location Systems. *J. Geophys. Res. Atmos.* **2016**, *121*, 895–911. [CrossRef]
14. Dowden, R.L.; Brundell, J.B.; Rodger, C.J. VLF Lightning Location by Time of Group Arrival (TOGA) at Multiple Sites. *J. Atmos. Sol.-Terr. Phys.* **2002**, *64*, 817–830. [CrossRef]
15. Said, R.K.; Inan, U.S.; Cummins, K.L. Long-Range Lightning Geolocation Using a VLF Radio Atmospheric Waveform Bank. *J. Geophys. Res. Atmos.* **2010**, *115*, D23108. [CrossRef]
16. Xu, X.; Huang, L.; Wang, S.; Ji, Y.; Liu, X.; Fang, G. VLF/LF Lightning Location Based on LWPC and IRI Models: A Quantitative Study. *Remote Sens.* **2022**, *14*, 5784. [CrossRef]
17. Zhang, J.; Zhou, J.; Li, J.; Gu, J.; Zhang, Q.; Dai, B.; Wang, Y.; Wang, J.; Zhong, Y.; Li, Q. Location Accuracy Improvement of Long-Range Lightning Detection Network in China by Compensating Ground Wave Propagation Delay. *Remote Sens.* **2022**, *14*, 3397. [CrossRef]
18. Gu, J.; Zhang, Q.; Li, J.; Zhang, J.; Zhou, J.; Dai, B.; Sun, H.; Wang, Y.; Wang, J.; Zhong, Y.; et al. Effect of Number and Configuration of Participating Stations on Lightning Location outside the Network. *Remote Sens.* **2022**, *14*, 4242. [CrossRef]
19. Zhu, Y.; Lyu, W.; Cramer, J.; Rakov, V.; Bitzer, P.; Ding, Z. Analysis of Location Errors of the U.S. National Lightning Detection Network Using Lightning Strikes to Towers. *J. Geophys. Res. Atmos.* **2020**, *125*, e2020JD032530. [CrossRef]
20. Cooray, V.; Cooray, G. The Electromagnetic Fields of an Accelerating Charge: Applications in Lightning Return-Stroke Models. *IEEE Trans. Electromagn. Compat.* **2010**, *52*, 944–955. [CrossRef]
21. Thottappillil, R.; Rakov, V.A. On Different Approaches to Calculating Lightning Electric Fields. *J. Geophys. Res. Atmos.* **2001**, *106*, 14191–14205. [CrossRef]
22. Baba, Y.; Rakov, V.A. Electromagnetic Models of the Lightning Return Stroke. *J. Geophys. Res. Atmos.* **2007**, *112*, D04102. [CrossRef]
23. Cooray, G.; Cooray, V. Electromagnetic Fields of a Short Electric Dipole in Free Space-Revisited. *Prog. Electromagn. Res.* **2012**, *131*, 357–373. [CrossRef]
24. Rakov, V.A.; Uman, M.A. *Lightning: Physics and Effects*; Cambridge University Press: Cambridge, UK, 2003. [CrossRef]
25. Cooray, V.; Cooray, G. Application of Electromagnetic Field Expressions of Accelerating Charges to Obtain Electromagnetic Fields of Engineering Return Stroke Models. *Electr. Power Syst. Res.* **2025**, *243*, 111429. [CrossRef]
26. Nucci, C.A.; Diendorfer, G.; Uman, M.A.; Rachidi, F.; Ianoz, M.; Mazzetti, C. Lightning Return Stroke Current Models with Specified Channel-Base Current: A Review and Comparison. *J. Geophys. Res. Atmos.* **1990**, *95*, 20395–20408. [CrossRef]
27. De Conti, A.; Silveira, F.H.; Visacro, S.; Cardoso, T.C.M. A Review of Return-Stroke Models Based on Transmission Line Theory. *J. Atmos. Sol.-Terr. Phys.* **2015**, *136*, 52–60. [CrossRef]
28. Cooray, V.; Cooray, G. Electromagnetic Fields of Accelerating Charges: Applications in Lightning Protection. *Electr. Power Syst. Res.* **2017**, *145*, 234–247. [CrossRef]
29. Cooray, V.; Cooray, G. A Novel Interpretation of the Electromagnetic Fields of Lightning Return Strokes. *Atmosphere* **2019**, *10*, 22. [CrossRef]
30. Hill, D.A.; Wait, J.R. Ground Wave Attenuation Function for a Spherical Earth with Arbitrary Surface Impedance. *Radio Sci.* **1980**, *15*, 637–643. [CrossRef]

31. Wait, J.R.; Hill, D.A. Ground Wave of an Idealized Lightning Return Stroke. *IEEE Trans. Antennas Propag*. **2000**, *48*, 1349–1353. [CrossRef]
32. Shoory, A.; Mimouni, A.; Rachidi, F.; Cooray, V.; Rubinstein, M. On the Accuracy of Approximate Techniques for the Evaluation of Lightning Electromagnetic Fields along a Mixed Propagation Path. *Radio Sci*. **2011**, *46*, RS2001. [CrossRef]
33. Moosavi, S.H.S.; Moini, R.; Sadeghi, S.H.H.; Kordi, B. Application of the Nonlinear Antenna Theory Model to a Tall Tower Struck by Lightning for the Evaluation of Return Stroke Channel Current and Radiated Electromagnetic Fields. *J. Geophys. Res. Atmos*. **2011**, *116*, D11118. [CrossRef]
34. Delfino, F.; Procopio, R.; Rossi, M.; Rachidi, F. Influence of Frequency-Dependent Soil Electrical Parameters on the Evaluation of Lightning Electromagnetic Fields in Air and Underground. *J. Geophys. Res. Atmos*. **2009**, *114*, D11113. [CrossRef]
35. Zhang, G.; Chen, M.; Wang, S.; Gao, Y.; Du, Y.-P. A New FDTD Model for Lightning Return Stroke Channel Above Lossy Ground and Its Validation with Rocket-Triggered Lightning Data. *IEEE Access* **2023**, *11*, 84475–84486. [CrossRef]
36. ITU-R. *Recommendation P.832–4: World Atlas of Ground Conductivities*; International Telecommunication Union: Geneva, Switzerland, 2015. Available online: https://www.itu.int/rec/R-REC-P.832-4-201507-I/en (accessed on 14 August 2026).
37. ITU-R. *Recommendation P.368–10: Ground-Wave Propagation Prediction Method for Frequencies between 10 kHz and 30 MHz*; International Telecommunication Union: Geneva, Switzerland, 2022. Available online: https://www.itu.int/rec/R-REC-P.368-10-202208-I/en (accessed on 14 August 2026).
38. Zhang, G. Study of the Effect of Observation Site and Propagation Path on Lightning-Produced Electromagnetic Pulse (LEMP) Based on Rocket-Triggered Lightning Data and FDTD Code. Ph.D. Thesis, The Hong Kong Polytechnic University, Hong Kong, China, 2023. Available online: https://theses.lib.polyu.edu.hk/handle/200/12708 (accessed on 14 August 2026).

Disclaimer/Publisher's Note: The statements, opinions and data contained in all publications are solely those of the individual author(s) and contributor(s) and not of MDPI and/or the editor(s). MDPI and/or the editor(s) disclaim responsibility for any injury to people or property resulting from any ideas, methods, instructions or products referred to in the content.